Stress/pressure-stabilized cubic polymorph of Li3Sb with improved thermoelectric performance

Mujde Yahyaoglu, Thomas Soldi, Melis Ozen, Christophe Candolfi, G. Jeffrey Snyder, Umut Aydemir

ARTICLE

Stress/Pressure-Stabilized Cubic Polymorph of Li_3Sb with Improved Thermoelectric Performance

Received 00th January 20xx,
Accepted 00th January 20xx

DOI: 10.1039/x0xx00000x

Mujde Yahyaoglu,[a,b,‡] Thomas Soldi,[c,‡] Melis Ozen,[a,b] Christophe Candolfi,[d] G. Jeffrey Snyder,*[c] Umut Aydemir*[b,e]

Li_3Sb has two polymorphs crystallizing in a face-centered cubic cell (c-Li_3Sb; BiF_3 structure type; space group $Fm\bar{3}m$) and in a hexagonal unit cell (h-Li_3Sb; Na_3As structure type; space group $P6_3/mmc$). c-Li_3Sb was predicted to be a promising thermoelectric material based on recent first-principles studies; however, the experimental transport characteristics have remained unknown so far. Herein, successful preparation of the c-Li_3Sb is reported by stress-induced mechanochemical synthesis (high-energy ball milling) along with its high-temperature thermoelectric properties. The hexagonal Li_3Sb (h-Li_3Sb) was revealed to be the stable phase at ambient conditions, while it starts unexpectedly transforming to the c-Li_3Sb by ball milling or under 60 MPa applied pressure at room temperature. Transport properties measurements performed on two polycrystalline specimens evidence that c-Li_3Sb behaves as a *p*-type degenerate semiconductor due to the formation of Li vacancies. In agreement with lattice dynamics calculations, c-Li_3Sb exhibits very low lattice thermal conductivity despite the lightweight of Li. A peak zT value of up to 0.4 at 625 K was achieved. Modelling suggests that the hole concentration should be reduced through aliovalent substitutions or under Li-rich conditions for further optimization. Although the strong air sensitivity of Li_3Sb makes its use in thermoelectric applications challenging, this simple superionic binary provides an attractive experimental platform to elucidate the effect of stress/pressure on phase transition as well as Fermi surface complexity on thermoelectric properties.

Introduction

Global demand for alternative energy resources other than fossil fuels has been amplified due to their depletion sources and environmental impacts of their consumption. The recent assessment uncovers that 72 % of the global energy consumption is lost during energy conversion steps.[1] The significant loss is specified as waste heat, which needs to be recovered so as to achieve improved global energy sustainability. Therefore, thermoelectric (TE) materials have gained great interest as a sustainable and reliable energy source by converting waste heat into electricity and functioning as vibration- and noise-free solid-state coolers.[2] The thermoelectric efficiency depends on the dimensionless thermoelectric figure of merit, $zT = \alpha^2\sigma T/\kappa$, where α, σ, T and κ are the Seebeck coefficient, electrical conductivity, absolute temperature, and total thermal conductivity, respectively.[3] Thermoelectric efficiency of the materials can be enhanced by maximizing the quality factor B, which is determined by the weighted mobility μ_w that corresponds to the charge carrier mobility weighted by the density of electronic states.[4, 5] Achieving optimized μ_w requires fine tuning of the carrier concentration through doping. Simultaneously, the thermal conductivity ($\kappa = \kappa_e + \kappa_L$, where κ_e and κ_L are the electrical and lattice contributions, respectively[2, 6]) should be lowered through nanostructuring, alloying or decorating secondary phases at the grain boundaries that act as additional phonon scattering centers, so long as μ_w is not significantly reduced.[6]

Zintl compounds, classified as phonon-glass, electron-crystal (PGEC), are considered to be promising thermoelectric candidates for power generation applications at high temperatures.[7] Zintl cations constitute the “phonon-glass” characteristics due to their loosely-ionically-bonded nature, while anionic subunits forming the covalently bonded framework are responsible for the “electron-crystal” properties.[8-10] Owing to their rich and complex crystal structures with a high number of atoms in the unit cells, Zintl phases exhibit inherently low lattice thermal conductivities [11].

The transport properties of the ternaries $X_{14}MnSb_{11}$ (X = Ca, Yb),[10, 12, 13] $X_5Y_2Sb_6$ (X = Ca, Yb; Y = Al, Ga, In),[14, 15] XY_2Sb_2 (X = Ba, Ca, Sr, Eu, Yb; Y = Ga, Cd, Zn, Mn),[16-24] XMg_2Bi_2 (X = Ca, Eu, Yb),[25, 26] and binary Mg_3X_2 (X = Sb, Bi)[27-32] Zintl phases have been recently shown to be high-efficiency thermoelectric materials. Because of their propensity to show cation vacancies, most of these phases exhibit p-type semiconducting behaviour, with only a handful of them displaying n-type behaviour achieved by

[a] Graduate School of Sciences and Engineering, Koç University, Istanbul-34450, Turkey.
[b] Koç University Boron and Advanced Materials Application and Research Center (KUBAM), Istanbul-34450, Turkey.
[c] Department of Materials Science and Engineering, Northwestern University, Evanston, IL-60208, USA.
[d] Institut Jean Lamour, Université de Lorraine, Nancy Cedex 54011, France.
[e] Department of Chemistry, Koç University, Istanbul-34450, Turkey.
[‡] These authors contributed equally to this work.
Electronic Supplementary Information (ESI) available: [details of any supplementary information available should be included here]. See DOI: 10.1039/x0xx00000x

either phase boundary mapping, intrinsic or extrinsic doping.[33-35]

Along with ternary phases, binary Zintl compounds with cations from group I or II can also crystallize with complex structures preserving PGEC characteristics.[36] Recently, theoretical calculations on transport properties of lithium-based semiconductor materials revealed that phases containing heavy pnictogens such as Sb or Bi could be promising thermoelectric materials.[37] Up to date, only a few theoretical studies are available in the literature on this family of materials, which are less studied compared to other alkali pnictide compounds.[38-40] Among the possible Zintl phases, Li_3Sb emerges as a very promising candidate due to its superionic conductivity[41-43], calculated narrow bandgap of 0.68 eV and low lattice thermal conductivity κ_L of 2.2 W $m^{-1}K^{-1}$ at 300 K, which is significantly lower than $CoSb_3$ (11.5 W $m^{-1}K^{-1}$),[44] n-type half-Heusler $Hf_{0.75}Zr_{0.25}NiSn_{0.99}Sb_{0.01}$ phases (4.0 - 4.6 W $m^{-1}K^{-1}$),[45] and SiGe bulk alloys (2.4 - 28 W $m^{-1}K^{-1}$)[46]. Considering the low κ_L of Li_3Sb, further calculations predicted maximum zTs of 0.87 and 0.39 at 900 K in p-type and n-type Li_3Sb, respectively.[37] Further taking into account the effect of various scattering mechanisms and scattering time τ, zT values as high as 2.4 (1.2) with τ = 5 fs and $n \approx 1.8 \times 10^{20}$ cm^{-3} ($n \approx 6.5 \times 10^{19}$ cm^{-3}) and 3.2 (1.6) with τ = 9 fs and $n \approx 9.6 \times 10^{19}$ cm^{-3} ($n \approx 5.6 \times 10^{19}$ cm^{-3}) in *p*-type (*n*-type) materials were predicted at 900 K. All these theoretical findings suggest that both p- and n-type Li_3Sb can show high thermoelectric performance for optimized carrier concentrations.[37] These predictions have been very recently experimentally tested on cubic Li_3Bi (space group $Fm\bar{3}m$) and hexagonal Li_3Sb (h-Li_3Sb; space group $P6_3/mmc$), with a peak zT value of 0.3 at 780 K for the latter. These results suggest that the cubic polymorph of Li_3Sb may exhibit higher thermoelectric performance due to the complexity of the top of the valence bands consisting of three degenerate bands with different effective masses evidenced by electronic band structure calculations.[47] This non-trivial topology may result in a high number of warped, non-ellipsoidal Fermi surface that can be beneficial to achieve high zT values.[48, 49] In this paper, we experimentally assess the thermoelectric potential of c-Li_3Sb through a detailed investigation of its high-temperature thermoelectric properties measured on polycrystalline specimens prepared by high energy ball milling. We revealed that Li_3Sb undergoes a phase change from h-Li_3Sb to c-Li_3Sb either by ball milling or applying low pressures (as low as 60 MPa at room temperature), which is quite unusual for thermoelectric materials. Our results are further discussed in light of the recent study on h-Li_3Sb.[50]

Experimental Method

Li_3Sb samples were synthesized from high purity elemental lithium (Li, 99.9 %, Sigma Aldrich) and antimony shots (Sb, 99.999 %, Sigma Aldrich). First, Li was cut into very tiny pieces in an Argon-filled glovebox. Stoichiometric mixtures of starting elements were then loaded into stainless steel vials with two half-inch stainless-steel balls and sealed inside a glove box. Li_3Sb powder samples were obtained using SPEX 8000M Series MixerMill in 90 minutes (6 cycles of 15 min on/off). Dense pellets of as-obtained powders were prepared with both spark plasma sintering (SPS; at 673 K, 60 MPa, 10 minutes) and rapid hot pressing to compare the phase formation.[51] For transport property measurements, the powder samples were loaded into 1/2-inch diameter high-density graphite dies (POCO) and compacted into dense pellets by using direct current-induced hot press at 773 K for 1 h under 60 MPa pressure in Ar atmosphere. Phase purity and the samples' oxidation behavior on air were analyzed by X-ray diffraction (XRD) using Phillips X'Pert diffractometer. The phase stability of the c-Li_3Sb sample was determined by DSC/TG (NETZSCH STA 449 F3 Jupiter) measurement in a closed Nb ampoule. Electrical and thermal transport properties were measured from 325 to 675 K. The electrical resistivity (ρ) and Hall effect measurements were carried out by using the van der Pauw technique under a magnetic field of 2 T using pressure-assisted tungsten electrodes.[52] The Seebeck coefficients (α) of the materials were measured by using chromel-Nb thermocouples.[53] Thermal diffusivity, D, measurements were performed with a Netzsch LFA 457 laser flash apparatus. Thermal conductivity (κ) of the samples was calculated using the relation $\kappa = DC_Pd$, where C_P is the isobaric heat capacity estimated using the Dulong-Petit law and d is the experimental geometric density.

Results and Discussion

Phase transition and structural analysis

Li_3Sb is an extremely air- and moisture-sensitive material that needed special care in storing and handling. Therefore, all the XRD samples were prepared in the glove box using Polyimide (Kapton) films. The XRD patterns of as-synthesized powder (Figure 1 and S1) show that the target cubic phase has been obtained successfully after ball milling.

Li_3Sb crystallizes with two polymorphic forms: in a face-centered cubic cell (BiF_3 structure type; space group $Fm\bar{3}m$ (No. 225)) and in a hexagonal unit cell (Na_3As structure type; space group $P6_3/mmc$ (No.194)). In the structure of Li_3Sb, there are twelve atoms per cubic (Z = 4; Li1 at 4*b* (½, ½, ½), Li2 at 8*c* (¼, ¼, ¼), and Sb at 4*a* (0,0,0) sites) and eight atoms per hexagonal (Z = 2; Li1 at 2*b* (0, 0, ¼), Li2 at 4*f* (1/3, 2/3, 0.583), and Sb at 2*c* (1/3, 2/3, 1/4) sites) unit cells with experimental lattice parameters of a=6.576 (1) Å, and a = 4.689 (1) Å, c = 8.328 (1) Å, respectively (see Figure 2).[54, 55] Early phase diagram and battery studies about the stability of these phases with temperature yielded contradictory reports.[42, 54, 56-60] Some studies reported c-Li_3Sb as the stable low-temperature phase, while some others considered h-Li_3Sb as the stable one under ambient conditions. After high energy ball milling, our samples were all single-phase crystallizing in the c-Li_3Sb form. After annealing as-synthesized c-Li_3Sb sample at 650 K for four days, the sample has almost completely transformed to h-Li_3Sb with a minor c-Li_3Sb (Figure 1), which may indicate that the c-Li_3Sb is a metastable phase at ambient conditions. Beutl et al. correlated this behaviour with the pressure effect, claiming that moderate pressure/stress stabilizes the c-Li_3Sb, while stress

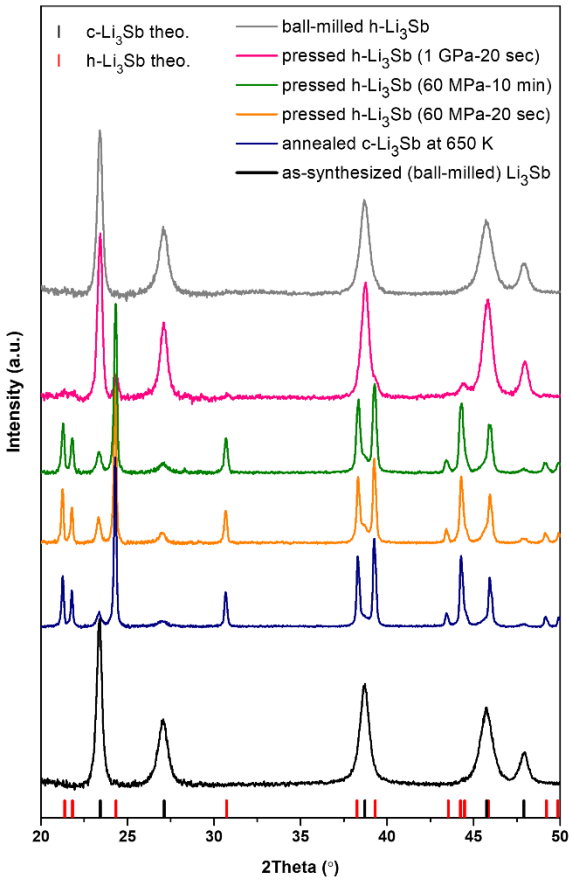

Figure 1. Experimental XRD patterns (Cu Kα) of as-syntesized Li_3Sb powder by high energy ball mill (black), c-Li_3Sb annealed at 650 K (blue), h-Li_3Sb hydrolic-pressed (orange: 60 MPa – 20 sec., green: 60 MPa – 10 min., pink: 1 GPa – 20 sec.), and h-Li_3Sb ball milled for 30 min. (grey) samples. Black and red ticks mark the calculated reflection positions of the c-Li_3Sb and h-Li_3Sb, respectively.

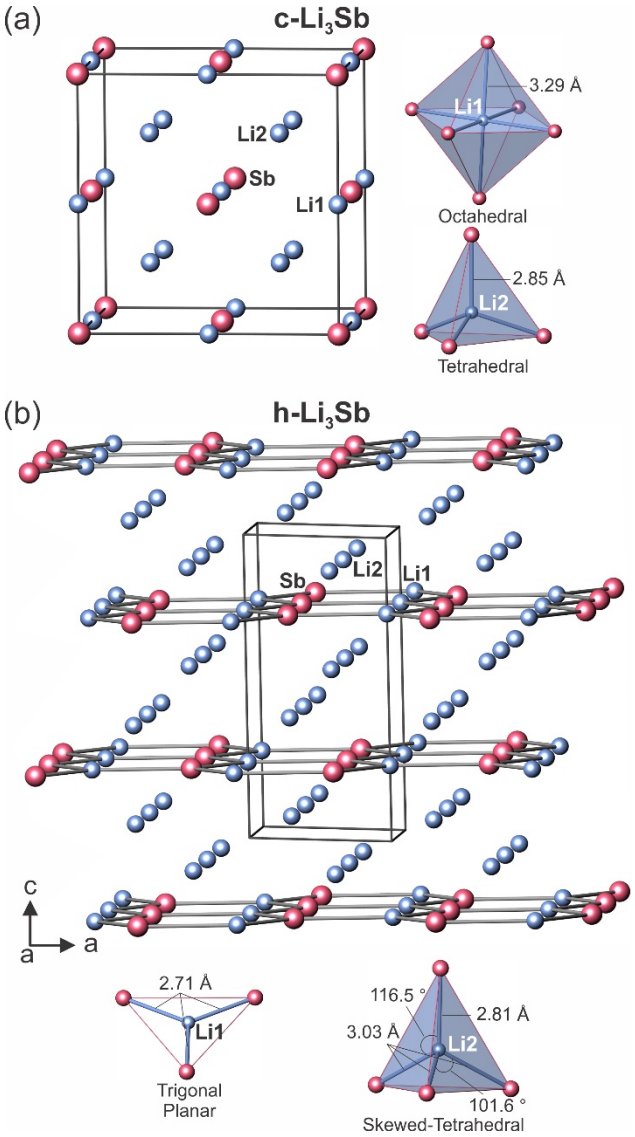

Figure 2. The Crystal structure of Li_3Sb. a) The cubic c-Li_3Sb phase has Face Centered Cubic (FCC) Sb with Li in both octahedral (Li1) and tetrahedral (Li2) interstices. b) The hexagonal h-Li_3Sb Hexagonal Close Packed (HCP) Sb with Li in trigonal (Li1) and skewed tetrahedral (Li2; one shorter, three longer bonds) interstices. Alternatively, the structure can be described as alternating planar Li1Sb layers stacking in ABAB sequence along the c-axis in which two layers of Li2 atoms are intercalated.

releasing processes such as thermal treatment leads to the formation of the h-Li_3Sb.[54] In similar systems of Li_3P, Na_3Sb, and Na_3Bi, only the hexagonal phase forms under ambient conditions,[56] whereas the cubic phase of Li_3P and Na_3Sb emerge only at higher pressures of around 1.3-3.3 GPa and 13 GPa, respectively.[57, 61] This correlates well with the total energy calculations indicating a small energy difference between the hexagonal and cubic phase of Li_3Sb (7 meV), whereas a larger one (131 meV) for the Na_3Sb.[62] Of note, Li_3Bi, Cs_3Bi, and Cs_3Sb crystallize only in the cubic structure.[63] With higher packing density, the cubic phase of Li_3Sb might indeed be stabilized under pressure, which was tested by pressing a sample consisting of mostly h-Li_3Sb by a hydraulic press at room temperature (see Figure 1). By applying 60 MPa pressure in a stainless-steel die (∅ = 10 mm), a small amount of h-Li_3Sb was transformed to the c-Li_3Sb after 20 sec. Almost the same amount was transformed at the same pressure after 10 min., signifying the transformation is time-independent and governed by the applied pressure. Almost complete phase transition took place under 1 GPa pressure in a stainless-steel die (∅ = 4 mm) after 20 sec. This explains well the existence of only the c-Li_3Sb after mechanochemical synthesis with ball milling. When a sample of h-Li_3Sb was ball milled for 30 min, a complete phase transformation to c-Li_3Sb was observed verifying that stress induced during high-energy ball milling stabilizes the c-Li_3Sb polymorph. The solid-state synthesis in Nb ampoules led to the formation of only h-Li_3Sb based on Peng *et al.*[50], which is expected for a stable low-temperature phase.

Regarding thermal stability of c-Li_3Sb, the DSC/TG thermogram in Figure S2 indicates one endothermic (ca. at 450 K) and one exothermic effect (ca. at 620 K) up to 673 K. No weight loss was observed based on the TG data. The peak at 450 K is attributed to either the melting point of pure Li (183.69 K)[64] or the eutectic temperature of the Li-rich phase (> 75 at. % Li)

as reported by Beuthl et al.[54] The exothermic peak at ca. $T_{onset} \approx$ 620 K is ascribed to the transformation of metastable c-Li_3Sb to stable h-Li_3Sb phase. These predictions were further verified with XRD analysis performed on the sample after the DSC/TG measurement (Figure S3). The XRD data shows that the starting cubic phase was almost completely transformed to the hexagonal one.

From a local structure analysis, it is apparent that very different Li environments exist for the two polymorphs of Li_3Sb (Figure 2). Li atoms in c-Li_3Sb have octahedral and tetrahedral coordination with Sb atoms, whereas they are coordinated in skewed tetrahedral and trigonal planar geometries in the h-Li_3Sb. Considering a very small ionic radius of Li^+ (0.76 Å; 6-fold coordination),[65] an octahedral hole could be too large to be positioned, which could be tested with the Pauling's rules on different coordination polyhedra.[66] For an octahedral environment, a r_{cation}/r_{anion} should be between 0.414 and 0.732. Taking the anionic radius of Sb^{3-} to be 2.23 Å,[67] a r_{cation}/r_{anion} of 0.34 is obtained, which is much lower than the stability limit. Therefore, Li^+ should be highly unstable in an octahedral environment in c-Li_3Sb and may distort to tetrahedral and trigonal planar sites in the h-Li_3Sb at ambient conditions which can lead to low thermal conductivity by a rattling-like mechanism (soft mode with high anharmonicity).[68] By applying low or moderate pressures, Li^+ in octahedral coordination might be restored with a metastable character.

After hot pressing, additional peaks of Li_2Sb and Sb are observed besides c-Li_3Sb, indicating Li loss during processing, which leaves Li-deficient phases Li_2Sb and elemental Sb in the samples (Figure S1). In this case, the phase composition shifts towards to Li-deficient region in the phase diagram.[54] Similar decomposition behaviour was observed in other experimental phase diagram studies for annealed samples,[54] in which an extremely high Li mobility may also contribute to this issue.[47, 69] The lattice parameter of Li_3Sb after ball milling, hot-pressing and transport property measurements was found to be a = 6.59448 Å, 6.5833(2) Å, and 6.5777(1) Å, respectively, indicating partial Li loss and/or phase decomposition as well. The XRD pattern for the SPS-sintered sample reveals a mixed-phase nature composed of h-Li_3Sb as the major phase while the c-Li_3Sb as the minor one (Figure S4). Considering the same pressure applied, the lower sintering temperature, current effect, and/or very short sintering time might result in a different phase formation behaviour than hot-pressed samples. In this study, all the transport properties were reported for the hot-pressed sample with the c-Li_3Sb as the only phase form of this system.

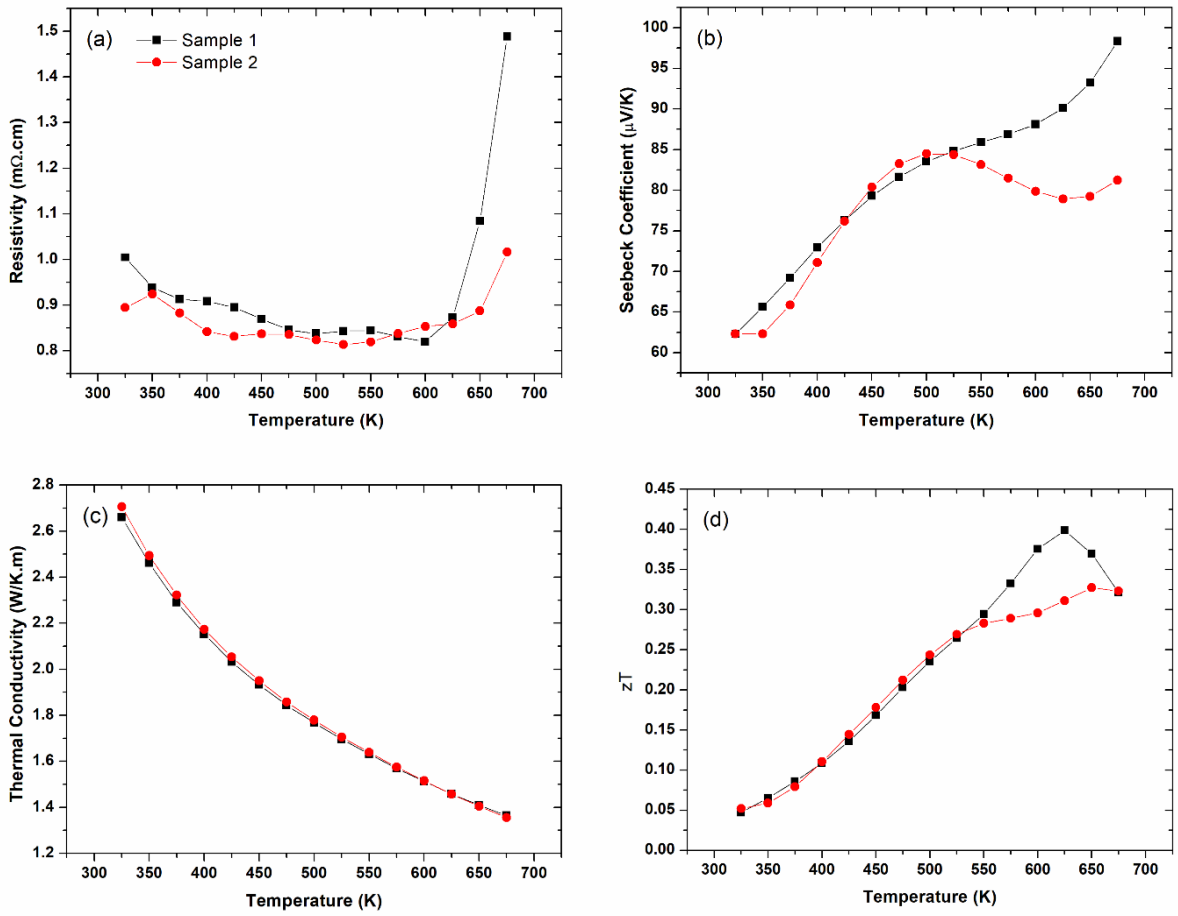

Figure 3. Temperature dependence of the a) electrical resistivity, b) Seebeck coefficient, c) total thermal conductivity, and d) thermoelectric figure of merit (zT) for the two Li_3Sb samples prepared.

Since Li_3Sb is an extremely air- and moisture-sensitive material, after air protective XRD measurement was done, Kapton foil was taken out from the sample holder and several 15-minute scans were performed to investigate the oxidation behaviour of the Li_3Sb powder in air under ambient conditions. The XRD pattern obtained during the first 15-minute scan reveals severe decomposition of Li_3Sb. As the exposure time increases, further deterioration is observed until the sample is almost fully oxidized and decomposed into Sb, $LiOH.H_2O$, and $LiSbO_3$ (Figure S5). Right before the transport measurements, the surfaces of the bulk pieces were slightly polished, however, partial surface oxidation couldn't be avoided.

Transport properties

The transport properties of the two identically prepared Li_3Sb samples were measured between 325 and 675 K. The temperature dependence of the electrical resistivity and Seebeck coefficients are presented in Figure 3a and 3b, respectively. The ρ values were found to be fairly constant up to 625 K for both samples. Above this temperature, the faster rise is probably due to either phase transition from c- to h-Li_3Sb or partial decomposition of Li_3Sb into Li_2Sb and Sb.[70] XRD analysis performed after measurement further confirms the formation of secondary phases (see Figure S1). Below 625 K, both samples display low ρ values ranging between 0.8 and 1.0 mΩ.cm over the entire temperature range. The low values measured indicate a degenerate behaviour, suggesting the presence of native defects. This finding is consistent with defect calculations indicating that acceptor-like Li vacancies acting as shallow acceptors are the most favorable defects due to their very low formation energy and the absence of competing electron-like defects.[47]

In agreement with the degenerate character, the values of the Seebeck coefficients (Figure 3b) remain moderate, increasing upon warming to ~85 μV.K^{-1} at 500 K. The positive α values indicate that holes are the main charge carriers, as observed in the hexagonal polymorph.

Figure 4a shows the hole concentration from the Hall effect of the two Li_3Sb samples as a function of temperature. The data measured on the two samples (low-temperature data for sample 1 and high-temperature data for sample 2) were combined to avoid inconsistent data points stemming from the difficulties in Hall-effect measurements for such an air-sensitive material. At room temperature, Li_3Sb has a relatively high hole concentration ($p \approx 0.5 \times 10^{20}$ h$^+$cm^{-3}), in agreement with its degenerate character.

The weighted mobilities μ_w were calculated from the measured α and ρ values (Figure 4b). μ_w has been shown to be proportional to the drift mobility, which is useful for identifying the dominant electron scattering mechanism in semiconductors.[4] In the case of Li_3Sb, the decreasing trend of μ_w with temperature indicates that electron-phonon scattering dominates. Grain boundary effects are likely not significant at high temperatures but may be contributing to the flattening of the curve near room temperature.

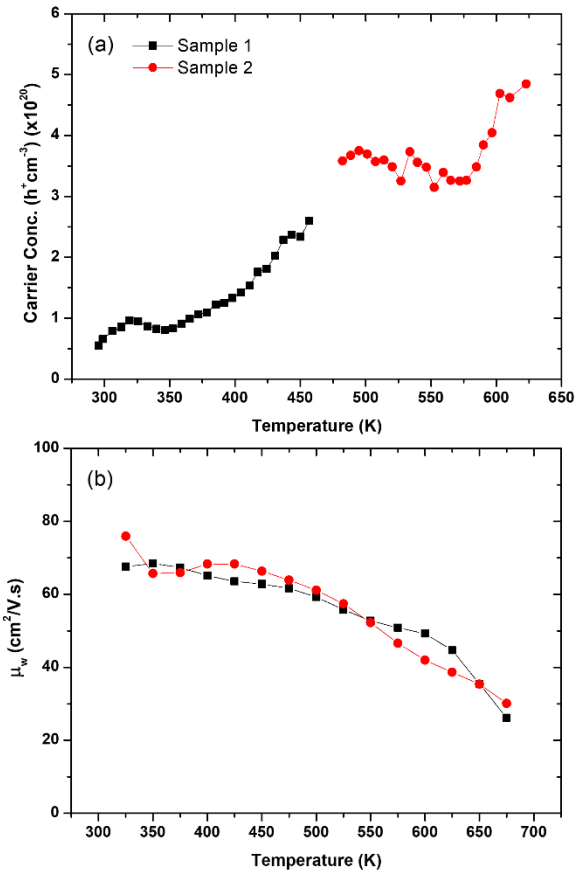

Figure 4. a) Carrier concentration and b) weighted mobility of Li_3Sb samples (Sample 1: black, Sample 2: red).

The density of states effective mass can be estimated from the measured Seebeck and Hall coefficients using an "effective mass" or often called "SPB" model.[71] The experimental Seebeck effective mass m_S^* is found to be $1.4m_e$. This is higher than the value determined by density functional theory calculations ($0.5m_e$).[47, 50]

In comparison to the experimental Seebeck values, α value at 500 K (85 μV.K^{-1}) was lower than the calculated value (170 μV.K^{-1}) predicted for *p*-type c-Li_3Sb at the same hole concentration (3×10^{20} h$^+$cm^{-3}).[37]

The mobility parameter μ_0 was extracted from:

$$\mu_w = \mu_0 \left(\frac{m_S^*}{m_e}\right)^{3/2} \qquad (2)$$

The μ_0 value of 39 cm^{2}V^{-1}s^{-1} at 400 K, calculated from the experimental hole concentration, Seebeck coefficients and electrical resistivity, compare very well with that determined by Ha et al. (40 cm^{2}V^{-1}s^{-1} at 400 K).[47]

The total thermal conductivities κ of the samples, with densities over 98% of the theoretical density, are shown in Figure 3c and S6. For all samples, κ decreases with increasing temperature following a T^{-1} law indicative of dominant phonon-

phonon Umklapp scattering. The SPS-treated sample has somewhat lower thermal conductivity values that could be due to the sample having both c- and h-Li_3Sb phases. The lattice thermal conductivity κ_L were calculated by subtracting the electronic thermal conductivity from κ. κ_e was calculated using the Wiedemann-Franz law $\kappa_e = L\sigma T$ where L is the Lorenz number, calculated from the SPB model to vary between 1.9 and 2.1×10^{-8} $W\Omega K^{-2}$ in the temperature range measured.[72] At 300 K, the κ_L values of around 2 W m^{-1} K^{-1} are consistent with lattice dynamics calculations for c-Li_3Sb[37] and with the experimental results obtained of Peng *et al* on hexagonal Li_3Sb.[50] These low values mainly originate from the large mass contrast between Li and Sb that contributes to low group velocities of the optical phonons as evidenced by the phonon calculations[50, 68]. Upon heating, κ_L rapidly decreases, following a trend similar to that calculated.[37] However, this model yields unphysical values above 625 K. We note that the phase decomposition, which is known to directly affect thermal diffusivity and specific heat measurements,[73, 74] occurs above these temperatures. Thus, the unphysical values reached near 625 K is not due to a problem in the measurement of the thermal diffusivity. This could be a consequence of a phase transition enthalpy and hence an overestimation of κ.[73]

Combined with the lattice thermal conductivity κ_l, μ_w determines the dimensionless material quality factor ($B \propto \mu_w/\kappa_l$), which provides an estimate for the peak zT achievable upon proper optimization of the carrier concentration. The experimental μ_w values inferred for Li_3Sb are relatively high compared to most of the *p*-type Zintl thermoelectrics.[34, 75-77]

Figure 3d shows the zT values of the Li_3Sb samples as a function of temperature. The highest zT of 0.4 was achieved for sample 1 at 625 K, which is higher than that achieved for hexagonal Li_3Sb (0.3 at 760 K). In addition, the hole concentration dependence of the zT calculated at 500 K by the SPB model (Figure 5b), shows that the experimental zT is consistent with these predictions. However, a peak zT of 0.7 is predicted for a hole concentration of 3.7×10^{19} cm^{-3}, that is, an order of magnitude lower than the experimental hole density achieved herein. Compared to the theoretical assumption of Yang et al., this predicted zT value at 500 K is significantly lower by 38 %.[37]

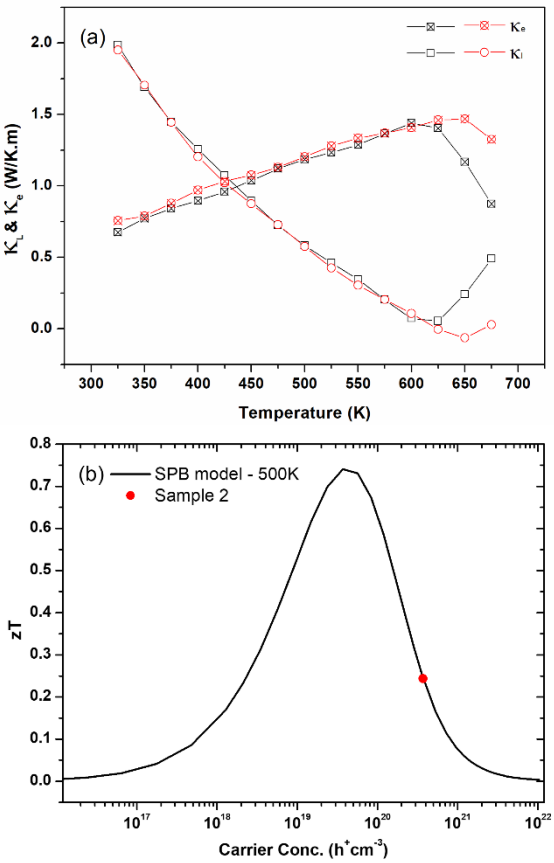

Figure 5. a) Lattice and electronic thermal conductivity as a function of temperature (Sample 1: black, Sample 2: red) and b) Model of zT showing that the carrier concentration is much higher than the optimum value (m^*_{SPB} = 1.4m_e, μ_0 = 38 $cm^2V^{-1}s^{-1}$).

Conclusions

Li_3Sb has been successfully prepared in the face-centered cubic structure with a mechanochemical route. A stress/pressure-induced phase transition was uncovered for this system, stabilizing the c-Li_3Sb metastable phase at low temperatures. The stability of the c-Li_3Sb may be improved by partial substitution of Cs for Li, and Bi for Sb as Li_3Bi, Cs_3Bi, and Cs_3Sb crystallize only in the cubic structure. Electrical resistivity measurements reveal a degenerate semiconducting behaviour with rather low resistivity values (0.8 and 1.5 mΩ.cm) and moderate Seebeck coefficients (60-100 μV.K^{-1}). The total thermal conductivity drops down to 1.35 W m^{-1} K^{-1} at 673 K, which is a relatively low value for such a lightweight material. A maximum zT of 0.4 was achieved at 625 K that is lower than the peak zT of 0.7 predicted by an SPB model for a hole concentration of 4×10^{19} h^+cm^{-3}. Higher zT values may be achieved in c-Li_3Sb upon further optimizing the hole concentration through doping studies. To be implemented in thermoelectric energy harvesting applications, airtight systems should be designed due to the extremely air-sensitive nature of this material.

Conflicts of interest

"There are no conflicts to declare".

Acknowledgements

U.A. gratefully acknowledges the financial support provided by the Scientific and Technological Research Council of Turkey (TÜBİTAK) with grant number 118M371. U. A. and C. C. acknowledge the financial support of the French Agence Nationale de la Recherche (ANR), through the PRCI project DENZIP (ANR-18-CE05-0042).

References

1. C. Forman, I. K. Muritala, R. Pardemann and B. Meyer, *Renewable and Sustainable Energy Reviews*, 2016, **57**, 1568-1579.
2. J. He and T. M. Tritt, *Science*, 2017, **357**, 1369.
3. F. J. DiSalvo, *Science*, 1999, **285**, 703-706.
4. G. J. Snyder, A. H. Snyder, M. Wood, R. Gurunathan, B. H. Snyder and C. Niu, *Advanced Materials*, 2020, **32**, 2001537.
5. S. D. Kang and G. J. Snyder, *Nature materials*, 2017, **16**, 252-257.
6. X.-L. Shi, J. Zou and Z.-G. Chen, *Chemical Reviews*, 2020, **120**, 7399-7515.
7. G. A. Slack, *CRC Handbook of Thermoelectrics*, 1995, 407-440.
8. D. M. Young and S. M. Kauzlarich, *Chemistry of materials*, 1995, **7**, 206-209.
9. F. Gascoin, S. Ottensmann, D. Stark, S. M. Haïle and G. J. Snyder, *Advanced Functional Materials*, 2005, **15**, 1860-1864.
10. S. R. Brown, S. M. Kauzlarich, F. Gascoin and G. J. Snyder, *Chemistry of materials*, 2006, **18**, 1873-1877.
11. E. S. Toberer, A. F. May and G. J. Snyder, *Chemistry of Materials*, 2010, **22**, 624-634.
12. S. R. Brown, E. S. Toberer, T. Ikeda, C. A. Cox, F. Gascoin, S. M. Kauzlarich and G. J. Snyder, *Chemistry of Materials*, 2008, **20**, 3412-3419.
13. Y. Hu, G. Cerretti, E. L. K. Wille, S. K. Bux and S. M. Kauzlarich, *Journal of Solid State Chemistry*, 2019, **271**, 88-102.
14. A. Zevalkink, G. S. Pomrehn, S. Johnson, J. Swallow, Z. M. Gibbs and G. J. Snyder, *Chemistry of Materials*, 2012, **24**, 2091-2098.
15. U. Aydemir, A. Zevalkink, A. Ormeci, H. Wang, S. Ohno, S. Bux and G. J. Snyder, *Dalton Transactions*, 2015, **44**, 6767-6774.
16. U. Aydemir, A. Zevalkink, A. Ormeci, Z. M. Gibbs, S. Bux and G. J. Snyder, *Chemistry of Materials*, 2015, **27**, 1622-1630.
17. U. Aydemir, A. Zevalkink, A. Ormeci, S. Bux and G. J. Snyder, *Journal of Materials Chemistry A*, 2016, **4**, 1867-1875.
18. X.-J. Wang, M.-B. Tang, H.-H. Chen, X.-X. Yang, J.-T. Zhao, U. Burkhardt and Y. Grin, *Applied Physics Letters*, 2009, **94**, 092106.
19. H. Zhang, M. Baitinger, M.-B. Tang, Z.-Y. Man, H.-H. Chen, X.-X. Yang, Y. Liu, L. Chen, Y. Grin and J.-T. Zhao, *Dalton Transactions*, 2010, **39**, 1101-1104.
20. H. Zhang, L. Fang, M.-B. Tang, H.-H. Chen, X.-X. Yang, X. Guo, J.-T. Zhao and Y. Grin, *Intermetallics*, 2010, **18**, 193-198.
21. H. Zhang, L. Fang, M.-B. Tang, Z. Man, H. Chen, X. Yang, M. Baitinger, Y. Grin and J.-T. Zhao, *The Journal of chemical physics*, 2010, **133**, 194701.
22. H. Zhang, M.-B. Tang, W. Schnelle, M. Baitinger, Z.-Y. Man, H.-H. Chen, X.-X. Yang, J.-T. Zhao and Y. Grin, *Journal of electronic materials*, 2010, **39**, 1772-1776.
23. H. Zhang, J.-T. Zhao, Y. Grin, X.-J. Wang, M.-B. Tang, Z.-Y. Man, H.-H. Chen and X.-X. Yang, *The Journal of chemical physics*, 2008, **129**, 164713.
24. A. Zevalkink, W. G. Zeier, E. Cheng, J. Snyder, J.-P. Fleurial and S. Bux, *Chemistry of Materials*, 2014, **26**, 5710-5717.
25. J. Shuai, H. Geng, Y. Lan, Z. Zhu, C. Wang, Z. Liu, J. Bao, C.-W. Chu, J. Sui and Z. Ren, *Proceedings of the National Academy of Sciences*, 2016, **113**, E4125-E4132.
26. A. F. May, M. A. McGuire, D. J. Singh, J. Ma, O. Delaire, A. Huq, W. Cai and H. Wang, *Physical Review B*, 2012, **85**, 035202.
27. J. Zhang, L. Song, S. H. Pedersen, H. Yin and B. B. Iversen, *Nature communications*, 2017, **8**, 1-8.
28. H. Tamaki, H. K. Sato and T. Kanno, *Advanced Materials*, 2016, **28**, 10182-10187.
29. C. L. Condron, S. M. Kauzlarich, F. Gascoin and G. J. Snyder, *Journal of Solid State Chemistry*, 2006, **179**, 2252-2257.
30. J. Mao, Y. Wu, S. Song, Q. Zhu, J. Shuai, Z. Liu, Y. Pei and Z. Ren, *ACS Energy Letters*, 2017, **2**, 2245-2250.
31. J. Mao, H. Zhu, Z. Ding, Z. Liu, G. A. Gamage, G. Chen and Z. Ren, *Science*, 2019, **365**, 495-498.
32. M. Ozen, M. Yahyaoglu, C. Candolfi, I. Veremchuk, F. Kaiser, U. Burkhardt, G. J. Snyder, Y. Grin and U. Aydemir, *Journal of Materials Chemistry A*, 2021, **9**, 1733-1742.
33. P. Gorai, A. Goyal, E. S. Toberer and V. Stevanovic, *Journal of Materials Chemistry A*, 2019, **7**, 19385-19395.
34. S. Ohno, K. Imasato, S. Anand, H. Tamaki, S. D. Kang, P. Gorai, H. K. Sato, E. S. Toberer, T. Kanno and G. J. Snyder, *Joule*, 2018, **2**, 141-154.
35. J. Q. Qu, V. Stevanovic, E. Ertekin and P. Gorai, *Journal of Materials Chemistry A*, 2020, **8**, 25306-25315.
36. S. M. Kauzlarich, S. R. Brown and G. J. Snyder, *Dalton Transactions*, 2007, 2099-2107.
37. X. Yang, Z. Dai, Y. Zhao, J. Liu and S. Meng, *Journal of Physics: Condensed Matter*, 2018, **30**, 425401.
38. J. Robertson, *Solid state communications*, 1983, **47**, 899-902.
39. S.-H. Wei and A. Zunger, *Physical Review B*, 1987, **35**, 3952.
40. M. Leonova, L. Sevast'yanova, O. Gulish and K. Burdina, *Inorganic materials*, 2001, **37**, 1270-1273.
41. A. Hu, W. Chen, X. Du, Y. Hu, T. Lei, H. Wang, L. Xue, Y. Li, H. Sun, Y. Yan, J. Long, C. Shu, J. Zhu, B. Li, X. Wang and J. Xiong, *Energy & Environmental Science*, 2021, **14**, 4115-4124.
42. W. Weppner and R. A. Huggins, *Journal of Solid State Chemistry*, 1977, **22**, 297-308.
43. V.-A. Ha, G. Yu, F. Ricci, D. Dahliah, M. J. van Setten, M. Giantomassi, G.-M. Rignanese and G. Hautier, *Physical Review Materials*, 2019, **3**, 034601.
44. W. Li and N. Mingo, *Physical Review B*, 2014, **89**, 184304.
45. G. Joshi, X. Yan, H. Wang, W. Liu, G. Chen and Z. Ren, *Advanced Energy Materials*, 2011, **1**, 643-647.
46. G. Joshi, H. Lee, Y. Lan, X. Wang, G. Zhu, D. Wang, R. W. Gould, D. C. Cuff, M. Y. Tang and M. S. Dresselhaus, *Nano letters*, 2008, **8**, 4670-4674.
47. V.-A. Ha, G. Yu, F. Ricci, D. Dahliah, M. J. van Setten, M. Giantomassi, G.-M. Rignanese and G. Hautier, *Physical Review Materials*, 2019, **3**, 034601.
48. N. A. Mecholsky, L. Resca, I. L. Pegg and M. Fornari, *Physical Review B*, 2014, **89**, 155131.
49. Z. M. Gibbs, F. Ricci, G. Li, H. Zhu, K. Persson, G. Ceder, G. Hautier, A. Jain and G. J. Snyder, *npj Computational Materials*, 2017, **3**, 1-7.
50. K. Peng, Z. Zhou, H. Wang, H. Wu, J. Ying, G. Han, X. Lu, G. Wang, X. Zhou and X. Chen, *Applied Physics Letters*, 2021, **119**, 033901.

51. A. D. LaLonde, T. Ikeda and G. J. Snyder, *Review of Scientific Instruments*, 2011, **82**, 025104.
52. K. A. Borup, E. S. Toberer, L. D. Zoltan, G. Nakatsukasa, M. Errico, J.-P. Fleurial, B. B. Iversen and G. J. Snyder, *Review of Scientific Instruments*, 2012, **83**, 123902.
53. S. Iwanaga, E. S. Toberer, A. LaLonde and G. J. Snyder, *Review of Scientific Instruments*, 2011, **82**, 063905.
54. A. Beutl, D. Cupid and H. Flandorfer, *Journal of Alloys and Compounds*, 2017, **695**, 1052-1060.
55. G. Brauer and E. Zintl, *Zeitschrift für Physikalische Chemie*, 1937, **37B**, 323-352.
56. J. Sangster and A. Pelton, *Journal of phase equilibria*, 1993, **14**, 514-517.
57. M. Leonova, I. Bdikin, S. Kulinich, O. Gulish, L. Sevast'Yanova and K. Burdina, *Inorganic materials*, 2003, **39**, 266-270.
58. L. Baggetto, P. Ganesh, C.-N. Sun, R. A. Meisner, T. A. Zawodzinski and G. M. Veith, *Journal of Materials Chemistry A*, 2013, **1**, 7985-7994.
59. M. Saubanère, M. B. Yahia, F. Lemoigno and M.-L. Doublet, *Journal of Power Sources*, 2015, **280**, 695-702.
60. G. Brauer and E. Zintl, *Zeitschrift für physikalische Chemie*, 1937, **37**, 323-352.
61. R. A. Leversee, K. Rode, E. Greenberg, V. B. Prakapenka, J. S. Smith, M. Kunz, C. J. Pickard and E. Stavrou, *Journal of Materials Chemistry A*, 2020, **8**, 21797-21803.
62. R. Caputo, *Journal of Electronic Materials*, 2016, **45**, 999-1010.
63. O. Madelung, in *Semiconductors: Data Handbook*, ed. O. Madelung, Springer Berlin Heidelberg, Berlin, Heidelberg, 2004, DOI: 10.1007/978-3-642-18865-7_16, pp. 437-445.
64. J. Emsley, *Oxford University Press, New York*, 1989.
65. R. D. Shannon, *Acta crystallographica section A: crystal physics, diffraction, theoretical and general crystallography*, 1976, **32**, 751-767.
66. L. Pauling, *The Nature of the Chemical Bond*, Cornell university press Ithaca, NY, 1960.
67. W. Peng, G. Petretto, G.-M. Rignanese, G. Hautier and A. Zevalkink, *Joule*, 2018, **2**, 1879-1893.
68. E. S. Toberer, A. Zevalkink and G. J. Snyder, *Journal of Materials Chemistry*, 2011, **21**, 15843-15852.
69. D. Chang, H. Huo, K. E. Johnston, M. Ménétrier, L. Monconduit, C. P. Grey and A. Van der Ven, *Journal of Materials Chemistry A*, 2015, **3**, 18928-18943.
70. A. Beutl, H. S. Effenberger and H. Flandorfer, *Zeitschrift für Kristallographie-Crystalline Materials*, 2017, **232**, 735-749.
71. A. Zevalkink, D. M. Smiadak, J. L. Blackburn, A. J. Ferguson, M. L. Chabinyc, O. Delaire, J. Wang, K. Kovnir, J. Martin and L. T. Schelhas, *Applied Physics Reviews*, 2018, **5**, 021303.
72. H. S. Kim, Z. M. Gibbs, Y. L. Tang, H. Wang and G. J. Snyder, *Apl Mater*, 2015, **3**, 041506.
73. M. T. Agne, P. W. Voorhees and G. J. Snyder, *Advanced Materials*, 2019, **31**, 1902980.
74. H. Chen, Z. Yue, D. Ren, H. Zeng, T. Wei, K. Zhao, R. Yang, P. Qiu, L. Chen and X. Shi, *Advanced materials (Deerfield Beach, Fla.)*, 2019, **31**, e1806518.
75. A. Zevalkink, G. Pomrehn, Y. Takagiwa, J. Swallow and G. J. Snyder, *ChemSusChem*, 2013, **6**, 2316-2321.
76. S. Chanakian, A. Zevalkink, U. Aydemir, Z. M. Gibbs, G. Pomrehn, J.-P. Fleurial, S. Bux and G. J. Snyder, *Journal of Materials Chemistry A*, 2015, **3**, 10289-10295.
77. E. S. Toberer, C. A. Cox, S. R. Brown, T. Ikeda, A. F. May, S. M. Kauzlarich and G. J. Snyder, *Advanced Functional Materials*, 2008, **18**, 2795-2800.